Title
Mode-specific vibrational predissociation dynamics of (HCl)2 via the free and bound HCl stretch overtones

Journal
The Journal of Chemical Physics, 152(19)

ISSN
0021-9606

Authors
Kapnas, Kara M
Murray, Craig

Publication Date
2020-05-21

DOI
10.1063/5.0003652

Peer reviewed

Mode-specific vibrational predissociation dynamics of $(HCl)_2$ via the free and bound HCl stretch overtones

Kara M. Kapnas and Craig Murray*

Department of Chemistry, University of California, Irvine, Irvine CA 92697, USA

* Email: craig.murray@uci.edu; Telephone: +1-949-824-4218

Abstract

Velocity-map ion imaging has been used to study the vibrational predissociation dynamics of HCl dimer following IR excitation in the HCl stretch overtone region near 1.77 Å. HCl monomer predissociation products were detected state-selectively using 2+1 resonance-enhanced multiphoton ionization spectroscopy. The IR action spectrum show the free HCl stretch ($2\nu_1$), the bound HCl stretch ($2\nu_2$), and a combination band involving the intermolecular van der Waals stretching mode ($2\nu_2+\nu_4$). Fragment speed distributions extracted from ion images obtained for a range of HCl(v = 0, 1; J) levels following vibrational excitation on the $2\nu_1$ and $2\nu_2$ bands yield the correlated product pair distributions. All product pairs comprise HCl(v = 1) + HCl(v = 0) and show a strong propensity to minimize the recoil kinetic energy. Highly non-statistical and mode-dependent HCl product rotational distributions are observed, in contrast to that observed following stretch fundamental excitation. Predissociation lifetimes are also mode-dependent: excitation of the free HCl leads to τ_{VP} = 13±1 ns, while the bound stretch has a shorter lifetime $\tau_{VP} \leq 6$ ns. The dimer dissociation energy determined from energy conservation, D_0 = 397±7 cm^{-1}, is slightly smaller than previously reported values. The results are discussed in the context of previous observations for $(HF)_2$ and $(HCl)_2$ after excitation of HX stretch fundamentals and models for vibrational predissociation.

Introduction

Hydrogen-bonded clusters have received a great deal of attention due to interest in their vibrational dynamics and predissociation behavior.[1–5] Hydrogen halide dimers in particular have served as prototypical systems for examining intermolecular forces and hydrogen bonding. In these simple systems, energy transfer following mode-specific vibrational excitation is inefficient, leading to remarkably long lifetimes and highly non-statistical product state distributions.[5,6] Detailed studies of dimer spectroscopy and vibrational predissociation dynamics are key to obtaining a better understanding of hydrogen-bonded networks in condensed phases and biological systems.

Ohashi and Pine recorded the first rotationally resolved spectrum of $(HCl)_2$ in the mid-IR using a long pathlength cooled cell under low pressure conditions;[7] they later inferred the dissociation energy to be D_0 = 431±22 cm^{-1} from IR transition intensities.[8] The spectrum suggested that the HCl monomer units undergo rapid interconversion tunneling. Further insight into the $(HCl)_2$ tunneling dynamics was provided by far-infrared absorption studies reported by both Blake *et al.*[9,10] and Mozzen-Ahmadi *et al.*[11,12] as well as coherent anti-Stokes Raman spectroscopy (CARS) studies by Furlan *et al.*,[13] who estimated a large ground state tunneling splitting of ~14.9 cm^{-1} and a substantially smaller fundamental HCl stretch tunneling splitting of ~3.4 cm^{-1}. Schuder *et al.*[14–16] later refined the rotational constants and interconversion tunneling frequencies for the free (ν_1) and bound (ν_2) HCl stretches of both $(HCl)_2$ and $(DCl)_2$ using a jet-cooled sample and high-resolution IR absorption spectroscopy. Combination bands of the van der Waals stretch (ν_4), geared bend (ν_5), and torsional (ν_6) modes have been reported and characterized by Fárník *et al.*[17,18] in the HCl stretch fundamental region. The experimental measurements have been accompanied by extensive *ab initio* calculations characterizing the potential energy surfaces for $(HCl)_2$ and larger clusters.[19–28]

A handful of experimental studies have explored the vibrational predissociation dynamics of the HCl dimer in the fundamental stretching region. Valentini and co-workers used stimulated Raman

excitation to excite ν_1 and ν_2 and probed the resulting HCl monomer fragments using resonance-enhanced multiphoton ionization (REMPI).[29,30] Photofragment recoil velocities were measured by displacing the pump and probe beams by a known distance,[31] and a refined value of the dissociation energy of D_0 = 439±1 cm^{-1} was determined from energy conservation, a value that is in excellent agreement with the value of 431±1 cm^{-1} later calculated by Mancini *et al*.[28] Predissociation lifetimes were found to be in the range 16–46 ns, with slower rates observed following excitation of the free HCl stretch, ν_1. The correlated HCl(v = 0, J) + HCl(v = 0, J) fragment rotational distributions showed a strong tendency to minimize recoil and maximize rotational excitation of the products. Vissers *et al.* obtained similar results using photofragment translational spectroscopy while complementary six-dimensional quantum calculations on the ES1–EL potential energy surface[19,20] predicted predissociation lifetimes and product state distributions that agreed qualitatively with experiments.[32] Vibrational predissociation of the more strongly bound $(HF)_2$ dimer (D_0 = 1062±1 cm^{-1}) after excitation of HF stretch fundamentals is similar, although a greater propensity for formation of high-J–low-J product pairs is observed and lifetimes are shorter.[33] The broader product rotational distributions and longer lifetimes observed in $(HCl)_2$ vibrational predissociation indicate a far less rigid structure, consistent with its larger tunneling splittings.[14,34]

Despite numerous spectroscopic studies of the fundamental region, the first overtone region has been neglected. Wittig and co-workers used IR cavity ring-down spectroscopy (CRDS) to record spectra of the $2\nu_1$ band of $(HCl)_2$ in a slit-jet expansion.[35] The $H^{35}Cl$–$H^{37}Cl$ and $H^{37}Cl$–$H^{35}Cl$ heterodimers remain distinguishable in the overtone spectrum indicating that interconversion tunneling is substantially quenched by HCl stretch vibrational excitation. This phenomenon has also been observed for both first and second overtone excitation of the HF stretching modes in $(HF)_2$.[34,36–38] Vibrational predissociation of $(HCl)_2$ following excitation in the HCl stretch overtone region has only been the (indirect) subject of a single study. Liu *et al*. examined vibrationally-mediated photodissociation of $(HCl)_2$ at 193 nm, measuring the total kinetic energy release using high-n

Rydberg H-atom time-of-flight spectroscopy.[39] The fastest moving H atoms observed at long IR–UV delays were attributed to photolysis of highly internally excited HCl(v = 0, J = 20, 21) produced by vibrational predissociation. Picconatto *et al*. subsequently investigated the 193 nm photodissociation of "untagged" $(HCl)_2$.[40] Without IR excitation, HCl products were formed almost exclusively in v = 0 with very little rotational excitation – the most populated level was $J \approx 2$. The apparent conversion of two quanta of vibrational excitation into monomer product rotation was surprising but these interesting observations have not been explored further.

Here, we present the results of infrared action spectroscopy and velocity-map ion imaging experiments characterizing the vibrational predissociation dynamics of $(HCl)_2$ in the HCl stretch overtone region near ~5650 cm^{-1} (~1.77 μm). IR action spectroscopy using 2+1 REMPI detection of HCl predissociation products has been used to identify the $2\nu_1$ and $2\nu_2$ overtone bands and the $2\nu_2+\nu_4$ combination band of $(HCl)_2$. Ion images have been recorded for a range of HCl(v = 0, 1; J) predissociation products following excitation on the $2\nu_1$ and $2\nu_2$ overtone bands, yielding correlated product pair state distributions.

Experimental methods

Experiments were performed in a velocity-map imaging (VMI) mass spectrometer that has been described in detail previously.[41] Briefly, HCl dimers were prepared in a supersonic expansion of 5% HCl in Ar (Airgas) from a stagnation pressure of 2 atm using a pulsed valve (General Valve, Series 9). The expansion was skimmed to produce a molecular beam, which was intersected by counter-propagating tunable IR pump and UV probe beams. The IR beam was generated using an optical parametric oscillator (OPO) system (Continuum Mirage 3000) pumped by a seeded Nd:YAG laser (Continuum Powerlite Precision 8010). While the OPO can produce single-mode output, only the non-resonant oscillator (NRO) and optical parametric amplifier (OPA) stages were pumped in the current experiments, providing a spectral linewidth of 4 cm^{-1} (FWHM). Average pulse energies in

the range 1.80–1.75 μm (5580–5700 cm^{-1}) were 10–13 mJ. The UV probe beam detected predissociation products via 2+1 REMPI and was generated by frequency doubling in BBO the visible output of a Nd:YAG-pumped dye laser (Continuum Surelite II–10, Quanta-Ray PDL-3) operating with Coumarin 480 or 500 dyes (Exciton). The probe laser produced UV pulses with a linewidth of 3 cm^{-1} (FWHM) and typical pulse energies of ~1 mJ. The IR pump and UV probe laser beams were focused at the center of the ionization region of the mass spectrometer using f = 250 mm fused silica lenses. For most measurements, the pump-probe time delay was fixed at 40 ns. Various IR-enhanced HCl REMPI transitions were observed in the vicinity of the E–X(0,0) and V–X(10,0) bands between 239.7–240.8 nm and on the F–X(0,1) band between 250. 0–251.1 nm. Product ions were accelerated by a stack of velocity-mapping electrodes towards a position-sensitive dual microchannel plate/phosphor screen assembly (Photonis, 40 mm diameter) and CCD camera (Basler A312f). The resulting images were analyzed using the polar onion-peeling method.[42] IR action spectra of $(HCl)_2$ were recorded with the UV probe laser fixed on a background-free HCl REMPI transition and monitoring the magnitude of the m/z = 35 and 36 peaks ($^{35}Cl^+$ and $H^{35}Cl^+$) in the mass spectrum while scanning the IR pump wavelength. The IR wavelength was calibrated by monitoring depletion of selected $F^1\Delta_2$–$X^1\Sigma^+$(0,0) REMPI signals while scanning over the P(1), R(0) and R(1) rovibrational transitions of the first overtone band at 5647 cm^{-1}, 5688 cm^{-1}, and 5706 cm^{-1}.

Results and Analysis

Initial measurements monitored depletion of the HCl monomer 2+1 REMPI signal as the IR wavelength was scanned and were used both to calibrate the IR OPO output wavelength and to quantify its bandwidth. Subsequently, the IR laser frequency was tuned to the peak of the sharp Q branch of the $2\nu_1$ band at 5656 cm^{-1} that was previously reported by Liu *et al.*[35] With the IR laser fixed at this frequency, the UV probe laser wavelength was scanned over a section of the Q branch of the $E^1\Sigma^+$–$X^1\Sigma^+$(0,0) band. The appearance of several additional lines in the REMPI spectrum and the

enhancement of others only when the IR pump laser preceded the UV probe laser confirmed predissociation. The REMPI spectra will be discussed in detail below, but in summary all the additional background-free lines observed in IR+UV experiments can be assigned to high-J levels of both v = 0, 1. Spectroscopic assignment of the background-free REMPI transitions is challenging as spectroscopic constants derived from jet-cooled spectra are unable to accurately predict transition frequencies for high-J levels. The relatively poor wavelength reproducibility of the dye laser compounds this difficulty. Conclusive assignments are made possible, however, by analysis of the ion images, which characterize the speed/translational energy and definitively identify the co-fragments. Since all product pairs identified comprise one HCl(v = 0, J) monomer and one HCl(v = 1, J), they are labelled as HCl(J_0,J_1), where the subscripts indicate the vibrational quantum number. The results of IR action spectroscopy, HCl product REMPI spectroscopy, and velocity-map ion imaging experiments will be described in turn below.

1. Infrared Action Spectroscopy

The IR action spectrum in the HCl stretch overtone region is shown in Figure 1. The spectrum was recorded by monitoring total m/z = 36 ($H^{35}Cl^+$) REMPI signal at a two-photon wavenumber of 83583 cm^{-1} while repeatedly scanning the IR laser over the range 5580–5700 cm^{-1}. The REMPI line is labeled as C in Figure 2 and was selected as one of the strongest background-free lines in the IR+UV REMPI spectrum. With knowledge of the photofragment speeds obtained from ion imaging experiments discussed below, it could be conclusively established that this transition originates in the J_1 = 12 level. Although it will not be discussed further, we note here that the relative magnitudes of the features in the IR action spectrum depend on the particular HCl product quantum state probed, suggesting strongly mode-specific predissociation dynamics.

The strongest vibrational band in Figure 1 is observed at 5656 cm^{-1} and is assigned to the $2\nu_1$ K_a = 1←0 sub-band of the $(H^{35}Cl)_2$ homodimer based on the CRDS spectrum of Liu *et al.*[35] While the

underlying rotational branch structure is unresolved due to the 4 cm^{-1} bandwidth of the IR laser, the equivalent $2\nu_1$ K_a = 1←0 sub-band of the $H^{35}Cl$–$H^{37}Cl$ heterodimer appears as a shoulder at lower frequency. The appearance of another weaker band at 5646 cm^{-1} is consistent with the energy spacing between the K_a = 1←0 and 0←0 sub-bands reported for the $(HCl)_2$ fundamental.[14] A similar pair of features are seen at 5597 cm^{-1} and 5607 cm^{-1}. The 10 cm^{-1} separation is consistent with assignment to the K_a = 1←0 and 0←0 sub-bands and they are assigned to the donor HCl stretching ($2\nu_2$) mode of the $(H^{35}Cl)_2$ homodimer. The weak shoulder on the $2\nu_2$ K_a = 0←0 sub-band located at 5592 cm^{-1} is attributed to the $H^{35}Cl$–$H^{37}Cl$ heterodimer.

Scanning the IR laser to the blue of the $2\nu_1$ transition revealed two new features at 5671 and 5683 cm^{-1}. The shift of ~75 cm^{-1} from the $2\nu_2$ band is consistent with the frequency for ν_4 determined from high-resolution IR absorption spectroscopy of the $\nu_2+\nu_4$ combination band in the fundamental region by Fárník *et al.*[18] We tentatively assign these features to the K_a = 0←0 and 1←0 sub-bands of the $2\nu_2+\nu_4$ combination band based on the frequency shift. We note however, that this assignment requires that the $2\nu_2+\nu_4$ combination band originate in the lower tunneling level; in contrast, the detailed spectroscopic analysis of Fárník *et al*. showed that the $\nu_2+\nu_4$ combination bands originated exclusively in the upper tunneling level.[18]

2. REMPI spectroscopy of HCl fragments

2+1 REMPI spectra of HCl were recorded over a section of the Q branch of the $E^1\Sigma^+$–$X^1\Sigma^+$(0,0) and the Q and P branches of the $F^1\Delta_2$–$X^1\Sigma^+$(0,1) bands (238.8–239.7 nm and 251.0–250.0 nm, respectively). The UV only spectrum shown at the bottom of Figure 2 results from background HCl(J_0) monomer. These lines are readily assignable to the Q and O branches of the E–X(0,0) band and the S(0) transition of the V–X(0,0) band, based on PGOPHER[43] simulations using rotational constants reported by Green *et. al.*[44] Transitions originating in J_0= 0–2 are far more intense and indicate a molecular beam temperature of ~12 K. The small residual population in higher rotational levels J_0 = 3–7 can be

characterized by an approximate rotational temperature of ~200 K. In contrast, the F–X(0,1) region is free of any detectable UV-only signal from HCl monomer.

IR+UV REMPI spectra of the E–X(0,0) Q branch region are shown in Figure 2, following excitation of the $2\nu_1$ $K_a = 1 \leftarrow 0$ sub-band at 5656 cm^{-1} and the $2\nu_2$, $K_a = 0 \leftarrow 0$ sub-band at 5597 cm^{-1}. In both cases, the IR laser bandwidth means that a range of J levels are excited. For convenience, these bands will be referred to simply as $2\nu_1$ and $2\nu_2$, and we neglect any effects of pumping the dimer to different K_a and J levels. The IR+UV spectra show marked enhancement of the E–X(0,0) Q(3)–Q(8) transitions and the degree is clearly dependent on the vibrational mode excited. For example, the Q(3), Q(6), and Q(7) lines show similar increases over background following $2\nu_1$ and $2\nu_2$ excitation. The Q(4) line doubles in intensity after $2\nu_1$ excitation, but displays more modest change after $2\nu_2$ excitation. The intensity of the Q(5) line is almost unchanged from the UV only background in both IR+UV spectra. Seven additional lines are also observed in the IR+UV REMPI spectra in this region. Three of these lines can be readily assigned to the Q(7), Q(8), and Q(9) transitions of the $V^1\Sigma^+$–$X^1\Sigma^+$(16,1) band based on simulations using published spectroscopic constants.[44,45] The lines labeled B, C, and F in Figure 2 could not be definitively assigned in this manner, although significant ion fragmentation to form Cl^+ suggests that they likely result from excitation to $^1\Sigma^+$ states.[44] The quantum states in which these transitions originate can be identified, however, through analysis of the speed distributions derived from the ion images. The assignments will be fully justified below, but here we simply state that line B results from $J_0 = 11$, line C probes $J_1 = 12$, and line F arises from $J_0 = 13$ products.

Figure 3 shows 2+1 REMPI spectra of the $F^1\Delta_2$–$X^1\Sigma^+$(0,1) band obtained with the IR tuned to the $2\nu_1$ and $2\nu_2$ bands. The ion yields were much lower in this region and the spectra are noisier than those shown in Figure 2 despite more signal averaging during acquisition, presumably due to a less favorable Franck-Condon factor. A strong, unresolved Q branch with a band head at $J = 14$ is evident in the IR-induced spectra at 79960–79985 cm^{-1}. The cluster of lines in the range 79700–79800 cm^{-1} are high-J transitions of the P branch. Small $m/z = 35$ (Cl^+) signals underlie the P(13), P(11) and

low-J Q branch transitions and are attributed to overlapping transitions to an unidentified $^1\Sigma^+$ state.[44] In contrast, ionization via the $F^1\Delta_2$ state does not result in any significant fragmentation. The relative intensities of the P branch lines are different following initial excitation of the $2\nu_1$ or $2\nu_2$ bands.

3. Ion imaging

Representative ion images obtained by monitoring HCl in the J_1 = 11–14 levels following initial excitation of the $2\nu_1$ and $2\nu_2$ modes of $(HCl)_2$ are displayed in the upper portion of Figure 4. The ion images display distinct isotropic rings and are characteristic of both the product quantum state probed and the particular overtone excited. Radial distributions are extracted from the ion images using the polar onion peeling approach and converted to speed distributions using a pixel-to-speed conversion factor of 6.089 m s^{-1} $pixel^{-1}$. The conversion factor was determined using calibration images of $S(^1D)$ obtained following photolysis of OCS at 235 nm and $Cl(^2P_{3/2})$ obtained from Cl_2 photolysis at 355 nm; both calibration measurements yielded consistent conversion factors. The fragment recoil speed distributions are also shown in Figure 4, below the respective ion images. Recoil speeds are modest, with most discernable features, corresponding to formation of different quantum states of the undetected $HCl(J_0)$ monomer, having speeds less than ~400 m s^{-1}. For the J_1 = 11–14 product levels, $2\nu_2$ excitation tends to lead to fewer features in the speed distributions, indicating a slightly narrower range of co-fragment product states.

The recoil speed distributions directly determine the correlated product pair distributions. From energy conservation:

$$h\nu_{IR} - D_0 = E_{V,R}(J_0, J_1) + E_T \quad (1)$$

where $h\nu_{IR}$ is the vibrational excitation energy, D_0 is the dimer dissociation energy, $E_{V,R}(J_0,J_1)$ is the rovibrational energy of the $HCl(J_0,J_1)$ product pair, and E_T is the recoil translational energy. The rovibrational term values for HCl are known to sub-wavenumber precision[45,46] and state-selective

REMPI detection precisely defines the contribution to $E_{V,R}(J_0,J_1)$ of the level probed. Consequently, the spacings between features in the speed distributions are directly related to the energy level spacing in the undetected HCl co-product.

Dissociation energy of $(HCl)_2$. Previous measurements have determined D_0 values of 431±22 cm^{-1} and 439±1 cm^{-1} for $(HCl)_2$.[8,30] These experimental results are in excellent agreement with a more recent theoretical value of 431±1 cm^{-1} calculated by Mancini *et al.*[27,28]] However, recoil speeds for different product pair combinations calculated using the more precisely determined experimental D_0 values were incompatible with the observed speed distributions. The discrepancies between the observed and calculated recoil speeds shown in Figure 4 imply a significant error in the available energy following predissociation. While one potential cause of the discrepancy is error in the pixel-to-speed calibration factor, which would introduce an error in E_T, we find that unreasonably large changes (>20%) would be necessary to achieve agreement. The revised calibration factor would be inconsistent with both independent calibration measurements. Another possible source of error is the IR photon energy. However, since the IR laser was calibrated by REMPI depletion measurements that involved scanning the IR frequency over well-known rovibrational transitions of the HCl monomer overtone band, we are confident that it is no larger than the laser bandwidth. Considering the terms in equation (1), the only remaining source of error is the previously reported value of D_0.

A non-linear least-squares fit was used to optimize D_0 by minimizing the root mean square differences between calculated speeds for each product pair in the distribution and the measured average speeds. The speed distributions were fit to sums of Gaussian functions each with fixed FWHM of 30 m s^{-1} (~5 pixels), characteristic of the experimental resolution, and the amplitudes and average speeds (peak centers) allowed to float. The D_0 fit was repeated for a total of fourteen different speed distributions for which spectroscopic assignments of the probed level could be made with confidence. Specifically, transitions probing J_1 = 7–9 and J_1 = 11–14 following vibrational

excitation of both $2\nu_1$ and $2\nu_2$ bands were used in the fit. Consistent values of D_0 were obtained with an average value of 397±7 cm^{-1} (1σ uncertainty). As can be seen in Figure 4, the new smaller value of D_0 reproduces all the features in the observed speed distributions and allows definitive assignment of the unidentified lines in the IR+UV REMPI spectra. Possible reasons for the discrepancy between the D_0 values obtained in this work and previously will be discussed below.

Assignments of unidentified REMPI features. Using the new, smaller value of D_0, the identities of the levels probed by the unidentified REMPI lines labeled B, C, and F in Figure 2 can be determined. The observed features in the speed distributions are readily matched to energetically allowed co-fragment HCl(J_v) levels. Ion images obtained probing on lines B and F are shown in Figure 5 along with their respective speed distributions and co-fragment assignments. Line B can be assigned to a REMPI transition that originates in J_0 = 11, with the undetected co-fragment being formed in J_1 = 7–9. Similarly, feature F is definitively assigned to a transition probing J_0 = 13, with the speed distributions indicating co-fragments formed in J_1 = 3–6. Satisfactory reproduction of the speed distribution obtained probing line C, which was used to measure the IR action spectrum shown in Figure 1, was obtained by assuming either J_0 = 20 or J_1 = 12 products. The rovibrational terms for these levels are 4489 cm^{-1} and 4480 cm^{-1}, respectively, hence both assignments are plausible, within the precision of the measurements, with HCl(J_0 = 6–8) co-products,. However, the speed distribution obtained from the line C ion image is the same as that obtained probing on the $F^1\Delta_2$–$X^1\Sigma^+$(0,1) P(12) transition shown in Figure 4 with regard to both peak heights and positions. Consequently, we favor the J_1 =12 assignment.

Correlated product pair and overall state distributions. The speed distributions directly identify the rotational distribution of the co-fragment formed in conjunction with the particular level probed. Most of the 2+1 REMPI transitions used for imaging probe HCl(J_1) product levels and the speed distributions directly provide the state correlated HCl(J_0) distributions. While in principle, the HCl(v

= 1) rotational population distribution, $P(J_1)$, can be derived from the 2+1 REMPI spectra of the F–X(0,1) band shown in Figure 3, empirical correction factors needed to convert REMPI signal intensities to populations are not known. Previously, Rudić *et al*. have determined correction factors for R-branch transitions of the F–X(0,0) band system with a room temperature sample but only for levels with $J \leq 11$.[47,48] The small Boltzmann populations in high-J levels and spectral congestion from transitions of the $d^3\Pi_0$–$X^1\Sigma^+$, $D^1\Pi$–$X^1\Sigma^+$, $f^3\Delta_2$–$X^1\Sigma^+$ and $V^1\Sigma^+$–$X^1\Sigma^+$(9,0) band systems make measurements of correction factors for the P-branch of the F–X(0,0) band impractical. Instead, we adopt an alternative approach to extract the populations that takes advantage of previous work finding J-independent correction factors (or assumed so) for the Q-branch of the E–X(0,0) band[28,49,50] and the pair-correlations that are determined unambiguously from the ion images.

The starting point is noting that the IR enhancements of the E–X(0,0) Q(3)–Q(7) lines shown in Figure 2 directly reflect the increased populations in the J_0 = 3–7 levels resulting from vibrational predissociation of the HCl dimer. We have assumed J-independent REMPI correction factors, in line with previous work.[28,49,50] Ion images acquired while probing high-J_1 levels via the F–X(0,1) band show that J_1 = 14 is formed in conjunction with J_0 = 2, 3, 4; J_1 =13 is formed with J_0 = 4, 5, 6; and so on. Correspondingly, images acquired probing J_0 = 4 products on the Q(4) line (for example) show only features that correspond to J_1 = 13, 14. The relative J_0 populations observed while monitoring high-J_1 levels can therefore be used as a simple basis and by varying the relative J_1 = 11–14 populations the Q-branch enhancements (i.e. the J_0 = 3–7 populations) can be reproduced. The effective empirical correction factors for the F–X(0,1) band derived in this way show that the detection sensitivity monotonically decreases for $J_1 > 11$. We assume unity for the few transitions from lower J_1 levels and propagate an estimated uncertainty of 20%. The V–X(16,1) spectrum in Figure 2 can be used to determine the relative populations in the J_1 = 7–9 levels and consequently the J_0 = 10–12 partners. Again, J-independent correction factors are assumed, [50] which is consistent with the constant Cl^+:HCl^+ fragmentation ratio observed in the spectra. The relative F–X(0,1) and V–X(16,1) band strengths are

unknown, but the presence of common product levels in each spectral region can be used to scale the populations derived from each spectrum. Transitions originating in J_1 = 7, 9 are used following $2\nu_1$ excitation and J_1 = 8 following $2\nu_2$ excitation to determine the scaling factors; in both cases the values are the same within the uncertainty of the measurements. Finally, lines B and F, identified as transitions to an unknown $^1\Sigma^+$ state and originating in J_0 = 11 and J_0 = 13, respectively, determine the relative populations in the J_1 = 3–9 levels. For all lines, the REMPI signal intensities were corrected for contributions from any underlying or unresolved REMPI transitions that manifest as additional features in the speed distributions. The overall P(J_0) and P(J_1) population distributions are self-consistent, indicating that the majority of the product population has been identified.

The correlated product pair distributions, $P(J_0,J_1)$ obtained following excitation to $2\nu_2$ and $2\nu_1$ are shown as intensity plots in Figure 6 and Figure 7, respectively. The product pair distributions appear as curved bands extending from high-J_1 and low-J_0 pairs at the bottom right corner to low-J_1 and high-J_0 pairs in the top left corner. The rapid decrease in intensity indicates that the latter are strongly disfavored for predissociation via both stretch overtones. Almost all product pairs have $J_1 > J_0$ following excitation of either the bound or free HCl stretch overtones of the dimer. The regions in the upper right corners comprise energetically inaccessible product pairs while the absence of population below the bands indicates that pairs with less rotational excitation (and consequently higher translational energy) are not populated. Summing horizontally or vertically gives the overall rotational distributions $P(J_0)$ or P(J_1), which are shown as bar charts. The product pair populations and their associated uncertainties are presented quantitatively in Table 1 and average values of J_1, J_0, and $|\Delta J|$ (where $\Delta J = J_1 - J_0$), compiled in Table 2, are identical within measurement uncertainty.

An alternative view of the product pair population distributions is presented in Figure 8, where ΔJ (assumed to be equivalent in magnitude to the recoil orbital angular momentum, $\Delta J = -L$) is plotted against the recoil translational energy, E_T. Accessible product pairs are shown as dots, while detected pairs are represented as circles, with areas proportional to their populations. The E_T axes for $2\nu_1$ and

313 $2\nu_2$ excitation are offset to account for the different amount of available energy (E_{AVL} = 5259 cm^{-1} or
314 5199 cm^{-1}, respectively) such that identical (J_0,J_1) pairs overlap. Figure 8 highlights some key
315 features of the product pair populaltion distributions. All detected product pairs have E_T < 600 cm^{-1}
316 and the vast majority have $\Delta J > 0$. Following $2\nu_1$ or $2\nu_2$ excitation, the average translational energy
317 has values $\langle E_T \rangle \approx$ 90 cm^{-1} or 60 cm^{-1}, indicating that only 1–2% of the available energy is partitioned
318 into translation. The product pair distributions determined following $2\nu_1$ and $2\nu_2$ excitation are
319 similar, although a few additional pairs are available for the former as a result of the larger E_{AVL}. For
320 the majority ΔJ > 0 population, sequences comprising constant values of J_1 form upward-curving arcs
321 as J_0 decreases. Along these arcs, the observed population generally decreases monotonically. For
322 example, the maximum population in the (J_0,14) sequences occurs for the highest energetically
323 accessible value of J_0, corresponding to (4,14) for $2\nu_1$ and (3,14) for $2\nu_2$, and decrease as J_0 decreases.
324 The same trend also holds for product pairs comprising J_1 = 11, 12, and 13. This trend is less distinct
325 for the minority $\Delta J < 0$ population, where the equivalent sequences of pairs with constant J_0 and
326 decreasing J_1 form downward-curving arcs in the lower half of the figure. Figure 8 also highlights
327 which product pairs are *not* observed. While the (J_0, 14) pairs account for almost half of the observed
328 products, the (14,J_1) pairs , which would have smiliar low-E_T values are not observed at all. Other
329 high-J_0 levels also contribute only marginally. No product pairs with $|\Delta J| >$12 are observed, and small
330 values are also disfavored, although in that case the larger differences in E_T between successive
331 members of the sequence means that compartively few pairs are accessible.

332 **4. Time dependence**

333 Vibrational predissociation lifetimes, τ_{VP}, of the $2\nu_1$ and $2\nu_2$ states have been determined by
334 measuring the dependence of the HCl REMPI signal as a function of time delay between the IR pump
335 and UV probe pulses. The time resolution of the measurements is limited by the temporal profile of
336 the laser pulses, which have FWHM of ~6 ns. Transient ion yields were measured for various

background free transitions in the E–X (0,0) region. The resulting time-dependent profiles were fit to the product of a single exponential rise and Heaviside step function, convoluted with a Gaussian function to mimic the instrument resolution.[51] Excitation of the acceptor HCl stretch overtone $2\nu_1$ led to a measurable time dependence – the vibrational predissociation lifetime is τ_{VP} = 13±1 ns (1σ uncertainty). In contrast, predissociation lifetime after excitation of the donor stretch $2\nu_2$ was shorter than the instrument resolution, leading to an upper limit of τ_{VP} < 6 ns. No *J* dependence could be identified.

Discussion

Overtone spectrum of $(HCl)_2$. The HCl stretch overtone of $(HCl)_2$ has been the subject of far less attention than the fundamental, with only the cavity ring-down spectrum of Wittig and co-workers appearing in the literature.[35] Jensen *et al*.[52] performed calculations on a six-dimensional *ab initio* potential energy surface to predict band origins of 5643 and 5609 cm^{-1} for the $2\nu_1$ and $2\nu_2$ modes, respectively, which are in reasonably good agreement with the experimental $2\nu_1$ and $2\nu_2$ band origins of 5656 cm^{-1} and 5597 cm^{-1}. The calculated transition dipole moments suggest the free HCl stretch overtone, $2\nu_1$, is approximately three times stronger than the bound HCl stretch overtone, $2\nu_2$.[52] The observed intensities in the IR action spectrum shown in Figure 1 cannot be compared directly without taking into account the HCl product state distributions resulting from the vibrational predissociation. The IR action spectrum was obtained probing J_1 = 12 and analysis of the population distributions (Figure 6 and Figure 7) show that the J_1 = 12 populations after excitation of $2\nu_1$ and $2\nu_2$ are the same within error (15±3 and 10±4, respectively, expressed as percentages). Consequently, the factor of two difference in the $2\nu_1$ and $2\nu_2$ integrated peak areas can be related directly to the relative transition strengths, which is in good agreement with the calculations.

The highest frequency features in the IR action spectrum at 5671 cm^{-1} and 5683 cm^{-1} are assigned to the $K_a = 0 \leftarrow 0$ and $K_a = 1 \leftarrow 0$ sub-bands of the $2\nu_2+\nu_4$ combination band, based on frequencies reported

by Fárník *et al.*[18] Four $\nu_2+\nu_n$ combination bands involving low frequency intermolecular modes of $(HCl)_2$ (plus those due to isotopologues) were observed in high-resolution spectra and assigned to the van der Waals stretch (ν_4) and geared bend motion (ν_5). Three out of four of the assignments were based on transitions originating from the upper tunneling level (permutation-inversion symmetry label B^+), which lies ~15 cm^{-1} above of the lower (A^+) level. Using a 3D quantum mechanical model, transition moments from the A^+ level were calculated to be 40 times weaker than corresponding transitions from the B^+ level, which was proposed to be a consequence of the extremely floppy nature of the dimer. In contrast, for the more rigid HF dimer several of the equivalent combination bands were observed originating from both tunneling components by Anderson *et al.*,[53] with the exception of the $\nu_2+\nu_4$ band, which was still only observed from the B^+ level. Interestingly, our $2\nu_2+\nu_4$ assignment only holds true if the transition originates from the lower tunneling state, suggesting that the relative intensities of overtone transitions originating from the A^+ state are larger. Application of the model used by Fárník *et al.*[18] to predict vibrational transition moments may shed light on the effects that can arise from overtone excitation. Higher resolution spectroscopic measurements would certainly allow for definitive assignments of the $(HCl)_2$ combination bands in this region of the spectrum.

Value of D_0. The bond dissociation energy of 395±7 cm^{-1} found in this work is ~40 cm^{-1} smaller than the theoretical value of 431±1 cm^{-1} calculated by Mancini *et al.*, which is in excellent agreement with previously reported experimental values for HCl dimer (the calculations also agree well with experimental measurements of D_0 for the HCl trimer).[28] Pine and Howard determined a value of D_0 = 431±22 cm^{-1} for $(HCl)_2$ from measured temperature-dependent IR line-strengths.[8] The value was later refined by Valentini and coworkers,[30,31] who used position-sensitive translational spectroscopy (POSTS) to directly measure the translational energy of HCl product pairs to obtain a more precise value of D_0 = 439±1 cm^{-1}. The POSTS method utilizes counterpropagating pulsed lasers (pump + probe) that are spatially separated by a known distance and fixed time delay.[54] By physically

scanning the distance between the pump and probe beams over hundreds of μm, the fragment spatial distributions and ultimately recoil velocities are measured. Product translational energies are obtained from simulations of the POSTS data that require precise knowledge of the time delay and spatial coordinates. While temporal jitter of the laser beams and uncertainties in spatial alignment can lead to errors, the temporal jitter of < 1 ns and the reported spatial uncertainty of ±2 μm would give rise to a small uncertainty in the speed of ~3 m s^{-1}, corresponding to the shortest time delay (0.8 μs) and smallest distance (300 μm). As in the velocity-map imaging measurements, the experimental observable in POSTS is the recoil speed distribution. In the current measurements, D_0 is determined directly from the radii of rings in the ion images and does not require precise knowledge of the time delay or spatial overlap between the two laser beams. As discussed earlier, potential sources of error in the VMI experiments arise from uncertainty in the pixel-to-speed calibration factor or the IR photon energy, neither of which are significant enough to account for the difference. Equation (1) neglects internal energy of the parent dimer and excitation of a hot band or high-J levels would lead to an apparent reduction in D_0. While incomplete cooling in the expansion is a possibility, this explanation is unsatisfactory. The same value of D_0 was determined following excitation of both $2\nu_1$ and $2\nu_2$ implying that the same hot band (or J levels) would have to be responsible at both IR excitation wavelengths, which seems improbable. Also, there are no internal degrees of freedom that provide the required ~40 cm^{-1} of additional energy. The frequencies of the intermolecular vibrational modes (ν_3–ν_6) determined from analysis of combination bands are too large (>60 cm^{-1}) while the tunneling splitting is too small (~15 cm^{-1}). The presence of sufficiently high-J levels ($J \approx$ 25) would result in broadened vibrational bands in spectrum, beyond the limitation of the laser bandwidth. The discrepancy in D_0 values appears, therefore, to be systematic but its origin is unclear.

Correlated product pair distributions. The ion imaging measurements characterize 22 distinct product pairs resulting from $2\nu_1$ predissociation and 20 from predissociation of $2\nu_2$. In all pairs identified, one of the HCl monomer products retains one quantum of vibrational excitation. This

observation is consistent with Ewing's selection rules for vibrational predissociation, which state that the change in effective quantum numbers is minimized.[55] In contrast, earlier experiments by Wittig and co-workers suggested the surprising result that vibrational predissociation of overtone excited $(HCl)_2$ led to the formation of highly rotationally excited HCl(J_0 = 20, 21),[39] for which energy conservation requires that the co-fragment be formed in v = 0. We find no conclusive evidence to support (J_0,J_0) pair formation following overtone predissociation of the HCl dimer. The most likely candidate in the 2+1 REMPI spectra is line C (indicated in Figure 2), for which J_0 = 20 and J_1 = 12 are equally plausible assignments. However, the relative magnitudes of the features in the speed distribution corresponding to the J_0 = 6, 7, 8 partner fragments are the same as those observed when probing J_1 =12 unambiguously on the F–X(0,1) P(12) transition. Formation of J_0 = 21 limits the partner monomer to $J_0 \leq 4$. The large background signals from residual monomer in the molecular beam makes probing low-J levels in v = 0 challenging but images obtained using the E–X(0,0) Q(3) and Q(4) transitions show no rings that could be attributed to J_0 = 21 co-fragments. In principle, REMPI detection of products is a more straightforward approach than that used in the earlier experiments, in which the H atoms produced by 193 nm photolysis of dimers, vibrationally excited dimers, and predissociation products were detected. Predissociation of the intermediate resonant states may well hinder direct detection of very high-J product levels, however.

The complete HCl(J_0,J_1) product pair population distributions shown in Figure 6, Figure 7, and Figure 8 have qualitatively the same shape for $2\nu_1$ and $2\nu_2$ predissociation, with a propensity to minimize the total translational energy release and form pairs with $J_1 > J_0$. For all product pairs observed, the fraction of the available energy partitioned into translation, $f_T = \langle E_T \rangle / E_{AVL} < 0.02$. The detailed $P(J_0,J_1)$ distributions for $2\nu_1$ and $2\nu_2$ excitation are somewhat distinct, however, which contrasts with the lack of mode-dependence observed by Valentini and co-workers after excitation of ν_1 and ν_2.[29,30] The linear surprisal analysis performed by Ni *et al.*[30] on the $P(J_0,J_0)$ distributions obtained following fundamental excitation resulted in a surprisal parameter of 39±5 for both ν_1 and ν_2, indicating large

deviation from the statistical prior. An equivalent analysis of the overtone data yields even larger positive surprisal parameters of 64±8 ($2\nu_1$) and 53±12 ($2\nu_2$), indicating even greater (and mode-specific) deviations from the statistical prior distribution and an even greater propensity for energy disposal into rotational motion rather than translation. However, the prior distribution is evaluated using three translational degrees of freedom and does not conserve angular momentum.[56] These deficiencies are corrected in phase space theory (PST), which correctly reduces the translational degrees of freedom to two and satisfies angular momentum conservation. Figure 9 compares the observed product pair distributions, plotted as $P(E_T)$, for $2\nu_1$ excitation, with the calculated statistical prior PST distributions. The results for $2\nu_2$ excitation are almost identical. The statistical calculations are constrained to only show (J_0,J_1) product pairs, which are calculated to account for only ~19% of the total distribution. The experimental product state distributions deviate significantly from both statistical models and show strong dynamical bias for energy disposal into rotational motion rather than translation.

The probability of formation of (J_0,J_1) product pairs can also be described using a simple momentum-gap model, as applied by Ni *et al.* in their analysis of predissociation via the stretch fundamentals:[30]

$$P(J_0,J_1) = \exp\left(-\mu v_{J_0,J_1}/a\right) \qquad (2)$$

Here, μ is the reduced mass, v_{J_0,J_1} is the recoil velocity of the particular (J_0,J_1) pair, and a is a normalization constant. A comparison of the experimental $P(J_0)$ and $P(J_1)$ distributions after $2\nu_1$ and $2\nu_2$ excitation with the predictions of the momentum-gap model is shown in Figure 6 and Figure 7, respectively. The momentum-gap model predicts broader $P(J_0)$ and $P(J_1)$ distributions than those observed experimentally. Specifically, it underpredicts the population in high-J_1 levels, and overpredicts the population in high-J_0 levels. As can be seen in Figure 8, accessible product pairs that would result in similarly modest E_T values are conspicuously absent (literarily, the dogs that did not bark) or strongly disfavored. The momentum-gap law does not distinguish between pairs with high-

J_1 that are observed and pairs with high-J_0 that are not. Other disfavored low-E_T pairs appear to be those that would result in either very large or very small values of $|\Delta J|$. For the former, the constraint is likely due to limitation on the orbital angular momentum, since $\Delta J = -L$. Large values of ΔJ require formation of either J_1 or J_0 levels that are near the limit of available energy, leaving insufficient energy available for recoil to generate enough compensatory orbital angular momentum. For small values of $|\Delta J|$, the accessible pairs are sparse, since both J_0 and J_1 must be similar in magnitude and relatively large to minimize E_T.

The quenching of interconversion tunneling suggests the dimer structure becomes more rigid after HCl stretch overtone excitation, and one might expect the dynamics to show similarities to the predissociation of $(HF)_2$.[34] Product pair distributions resulting from vibrational predissociation of $(HF)_2$ after excitation of the HF stretch fundamentals have been measured by Bohac *et al*.[33] While the rotational distributions also showed a strong propensity for small E_T, they could not be described by either a linear surprisal analysis or the momentum-gap model. Rather, the $P(J_0,J_0)$ distributions showed a propensity for formation of low-J_0–high-J_0 pairs, while $J_0 \approx J_0$ pairs were suppressed. The $(HF)_2$ predissociation data show statistically significant positive correlations between $P(J_0,J_0)$ and $|\Delta J|$, the absolute value of the difference in J_0 values for each pair. The low-J_0–high-J_0 pair propensity was interpreted as being a result of an impulsive dissociation in which the H-bond donor HF experiences a larger torque and becomes the high-J_0 product, while the acceptor HF experiences a small torque and becomes the low-J_0 fragment. Overtone excitation of $(HCl)_2$ leads to product pair distributions that show similar correlations between $P(J_0,J_1)$ and $|\Delta J|$. A key difference, however, is that excitation of the fundamental stretches in $(HF)_2$ restricts products to the vibrational ground state and renders the donor/acceptor indistinguishable while overtone excitation results in one fragment retaining one quantum of vibration. Within the impulsive model, one might expect $2\nu_2$ excitation to result in the donor being formed in $v = 1$ and the acceptor in $v = 0$, leading to pairs with ($J_1 > J_0$), and *vice versa* for $2\nu_1$ excitation ($J_1 < J_0$). Since almost all product pairs are formed with $J_1 > J_0$ for both

484 overtones, there appears to be no obvious association between the vibrationally excited fragment
485 and its role as either donor or acceptor. Trajectory calculations exploring the vibrational
486 predissociation of $(H_2O)_2$ after excitation of the donor OH stretch fundamental have shown that the
487 donor and acceptor moieties switch roles multiple times prior to dissociation,[57] which occurs with a
488 time constant of 80 ps. It is highly likely that similar interchange of donor and acceptor occurs in the
489 $(HCl)_2$ after overtone excitation, for which the predissociation lifetimes are significantly longer.

490 McCaffery and co-workers have developed a model for collision-induced rotational and vibrational
491 energy transfer,[58] and subsequently extended it to describe vibrational predissociation.[59] The model,
492 which is rooted in classical mechanics, is based on linear to angular momentum interconversion via
493 the short range repulsive part of the intermolecular potential. Diatomic molecules are modeled as
494 hard ellipses, with parameters determined from bond lengths. The model has successfully been used
495 in various contexts, including modeling the product rotational distributions arising from vibrational
496 predissociation of various weakly bound dimers.[60–62] Here, we apply it qualitatively to overtone
497 predissociation of HCl dimer with the simplifying assumption that dissociation leads to counter
498 rotation of the HCl monomers i.e. the orbital angular momentum of the products is equal and opposite
499 to the difference between the rotational angular momenta for the H-bond acceptor and donor
500 fragments:

$$\Delta J = J_{\mathrm{d}} - J_{\mathrm{a}} = -L \tag{3}$$

501 Trajectory calculations exploring the vibrational predissociation of $(H_2O)_2$ have found *J*–*J*
502 correlations that indicate the fragment *J* vectors are preferentially antiparallel.[57] Following the
503 approach taken for rotational transfer in diatom-diatom collisions,[63] we can write two separate "A-
504 equations" for the angular momentum generated in the H-bond acceptor and donor:

$$J_{\mathrm{a}} = \mu v_{\mathrm{r}} b_{\mathrm{n,a}}^{\mathrm{max}} \tag{4a}$$

$$J_{\mathrm{d}} = \mu v_{\mathrm{r}} b_{\mathrm{n,d}}^{\max} \tag{4b}$$

505 Here, μ is the reduced mass, v_{r} is the threshold or channel-opening velocity, and $b_{\mathrm{n}}^{\max}$ are the
506 maximum torque-arms for the H-bond acceptor and donor. The orbital angular momentum is
507 determined by the sum of the torque-arms:[63]

$$L = \mu v_{\mathrm{r}} \left(b_{\mathrm{n,d}}^{\max} + b_{\mathrm{n,a}}^{\max} \right) \tag{5}$$

508 The "E-equation" for vibrational predissociation is given simply by:

$$\Delta E_{J_0,J_1} = \frac{1}{2} \mu v_{\mathrm{r}}^2 \tag{6}$$

509 where $\Delta E_{J_0,J_1}$ is the energy gap from the initially excited dimer to a specific (J_0,J_1) product pair.

510 While the energy conserving threshold velocities are readily calculated using known HCl term values,
511 the slopes of the A-plots depend on the values of $b_{\mathrm{n}}^{\max}$. To estimate $b_{\mathrm{n}}^{\max}$, the monomers are modeled
512 as hard ellipses with semi-major and semi-minor axes related by $a = 2b$; the length of the semi-major
513 axis a is chosen to be equal to either the equilibrium bond length (r_{e} = 1.297 Å) or the outer turning
514 point of a vibrationally excited HCl molecule, which has been found empirically to be appropriate for
515 vibrational predissociation.[59] Outer turning point values of $r_{\max}$ = 1.393 Å, 1.496 Å, and 1.576 Å were
516 calculated for v = 0, 1, and 2 using LeRoy's program RKR1,[64] with Dunham coefficients reported by
517 Rank *et al.*[45] Figure 10 shows the dimer geometry, optimized at the MP2/aug-cc-pVDZ level of theory
518 using NWCHEM,[65] and identifies the coordinate system. As a heteronuclear diatomic, HCl has two
519 effective maximum torque-arms (corresponding to impulse at the H and Cl ends of the molecule). If
520 the angle θ is defined relative to the y-axis (minor axis) as shown in Figure 10, then $b_{\mathrm{n}}^{\max}$ can be
521 calculated using:[66]

$$b_{\mathrm{n}}^{\max} = \left| \frac{[(a^2 - b^2)\sin\theta - a x_0]\cos\theta}{\sqrt{a^2\cos^2\theta + b^2\sin^2\theta}} \right| \quad (7)$$

The ellipse is centered at the mid-point of the HCl bond, and x_0 is the displacement of the center of mass towards the Cl atom. The dependence of $b_{\mathrm{n}}^{\max}$ and θ on the angle α (the angle between the bond axis and the center of mass recoil) are shown Figure 10. Optimum values for $b_{\mathrm{n}}^{\max}$ for the donor and acceptor fragments are summarized in Table 3 alongside lower values that reflect the calculated dimer equilibrium geometry. As noted earlier, interchange of the donor and acceptor on the predissociation timescale is likely. The terms donor and acceptor are used here to refer to the fragments that access the long and short torque arms, respectively.

Figure 11 shows a velocity-angular momentum (v_{r}–J) plot for HCl dimer predissociation after excitation of the donor stretch overtone, $2\nu_2$; the equivalent diagram for $2\nu_1$ is very similar and modified only by the slight increase in E_{AVL} and choice of values for $b_{\mathrm{n}}^{\max}$. The A-plots for the donor and acceptor have been evaluated using the largest possible torque-arms of $b_{\mathrm{n,d}}^{\max}$ = 0.95 Å and $b_{\mathrm{n,a}}^{\max}$ = 0.22 Å, which corresponds to use of the outer turning point for v = 2 and v = 0 , respectively. Use of smaller values of the effective torque-arms that would be appropriate for the equilibrium geometry reduces the A-plot slopes (the effect is more dramatic for the acceptor). The E-plots are calculated for (J_0,J_0) and (J_0,J_1) products using rotational term values. The backward-arching shape is typical for vibrational predissociation and the E-plot for formation of (J_0,J_1) products terminates at the energetic threshold, where J_0 or J_1 = 14, while that for (J_0,J_0) extends to J_0 = 21. In both E-plots, the partner is implicitly formed in J = 0. For the donor (long torque arm), predissociation is energetically constrained for all but the highest J_{d} product levels (the E-plot lies at larger values of v_{r} than the A-plot). Simultaneously satisfying energy conservation requires a reduction in the effective torque-arm, which suppresses low-J_{d} channels in particular. For the acceptor fragment (short torque arm), linear to angular momentum conversion becomes the dominant constraint beyond J_{a} = 9 for (J_0,J_1) products and J_{a} = 14 for (J_0,J_0) products. Reduction of $b_{\mathrm{n,a}}^{\max}$ has a significant effect on the slope of the

acceptor A-plot and implies imposition of an even more stringent angular momentum constraint. The most probable product channels are those that most easily satisfy both angular momentum and energy requirements. For (J_0,J_0) pairs the v_r–J plot suggests that $J_d \approx 20$ is most probable, while for (J_0,J_1) pairs, $J_d \approx 13$ is most likely. Based on the experimental observations, J_d corresponds to J_1 (although the constraints are the same for J_0) since but it is clear that only the long torque-arm is able to generate the high-J_1 levels observed experimentally.

The v_r–J plot can be used to rationalize why (J_0,J_0) pairs are not observed experimentally (*pace* Liu *et al*.[39]). As noted by McCaffery and Marsh in their discussion of the predissociation of van der Waals complexes of OH with various partners,[59] vibrational excitation of one of the fragments can serve as a sink for a large fraction of E_{AVL} and significantly reduces the angular momentum load. We also show in Figure 11 a reduced E-plot for J_a products where the co-fragment is in $J_d = 20$ (such high J levels are inaccessible via the shorter acceptor torque-arm). The shallow acceptor A-plot indicates an upper limit of $J_a \leq 5$ (and much lower for smaller values of $b_{n,a}^{max}$ that would be more representative of the dimer geometry) and consequently requires a lower limit product orbital angular momentumof $|L| = |J_d - J_a| \geq 15$. Significant variation in the dimer geometry such that both monomer fragments can access the longer torque-arm would have only a small effect of reducing the lower limit to $|L| \geq 13$. The intermolecular potential is likely insufficiently anisotropic to generate such large values of L when using the combined torque-arm defined in Equation 7 and formation of (J_0,J_0) product pairs are strongly suppressed. We note that (J_0,J_1) product pairs with values of $\Delta J > 11$ are observed to have minimal populations (see Figure 8) and the average value is only ~8 (see Table 2).

Focusing first on $2v_2$ excitation, almost all experimentally observed (J_0,J_1) product pairs have $J_1 > J_0$, as shown in Figure 8. The difference in the slopes of the A-plots suggests that it is the donor fragment that must be formed with the larger value of J. The product pair with the greatest population is (6,13) and Figure 11 shows the reduced E-plot obtained when $J_1 = J_d = 13$. The reduced E-plot suggests that only $J_0 = J_a \leq 4$ channels are accessible if angular momentum is generated via the acceptor torque-

arm. However the (4,13) pair is formed with a population more than ten times smaller than (6,13), and (J_0,13) pairs with lower values of J_0 are not observed, a trend that can be justified by the momentum-gap law. The v_r–J plot implies that generation of J_0 = 5, 6 requires the system to access the longer torque arm, which may indicate signifcant rearrangement prior to predissociation and is consistent with interchange of the donor and acceptor fragments. In general, however, comparison of the overall $P(J_1)$ and $P(J_0)$ product state distributons shown in Figure 7 with the v_r–J plot shown in Figure 11 suggests a correspondence between J_1 and J_d and between J_0 and J_a. The cluster of most populated J_1 levels are consistent with the J_d channels that most readily satisfy energy and angular momentum constraints. Similarly, the most populated J_0 levels broadly coincide with the most accessible J_a channels indicated on the v_r–J plot. It seems reasonable to conclude that the dominant, although not exclusive, predissociation mechanism involves the donor HCl retaining one quantum of vibrational excitation. For the small subset of product pairs with $J_1 < J_0$, it seems likely that intramolecular vibrational energy redistribution (IVR) occurs but is incomplete on the predissociation timescale ($\tau_{vp} < 6$ ns).

One might expect the correspondence to be reversed following excitation of the free (acceptor) HCl stretch overtone, $2\nu_1$, and J_1 to be associated with the acceptor and J_0 with the donor. The v_r–J plot is qualitatively the same, with only slight changes due to the choice of maximum torque-arm and the available energy. However, the product pair distributions for $2\nu_1$ excitaiton also show a strong propensity for $J_1 > J_0$, indicating that once again it is the (nominal) H-bond donor fragment that is preferentially vibrationally excited. The longer predissociation lifetime τ_{vp} = 13 ns allows signifcantly more time for IVR and interchange of the donor and acceptor fragments, which might be expected to lead to roughly equal propensities for $J_1 < J_0$ pairs as for the dominant $J_1 > J_0$ pairs. It seems that localizing vibrational energy in the donor allows more efficient coupling to the continuum, and leads to the obsered strong propensity for $J_1 > J_0$. Further experiments focusing on vibrational excitation of the ($H^{35}Cl$–$H^{37}Cl$) heterodimers, coupled with mass-resolved detection of the monomer

predissociation products would allow direct measurements of the relationship between the particular mode excited and partitioning of the energy between rotational vibrational levels of the donor and acceptor fragments. Trajectory calculations would also be valuable.

Predissociation lifetimes: Vibrational predissociation lifetimes of τ_{VP} = 13±1 ns and < 6 ns were determined from the appearance times of HCl products after excitation of $2\nu_1$ and $2\nu_2$, respectively; the latter measurement is an upper limit defined by the laser pulse duration. The predissociation lifetimes are significantly shorter than those observed after fundamental excitation, where linewidth measurements indicated values of $\tau_{VP} \geq 100$ ns for ν_1 and 31±7 ns for ν_2.[14] Direct measurements of HCl appearance times after ν_2 excitation by Ni *et al.*[30] were broadly consistent with the linewidth measurements, but found a shorter lifetime for ν_1 excitation. Observation of faster rates after excitation of the upper tunneling component associated with ν_2 excitation suggests some degree of mode specificity. The faster predissociation rates observed after excitation of the bound HCl stretch overtone can be explained by its stronger coupling to the intermolecular van der Waals dissociation coordinate.[1,2] The predissociation lifetimes of $(HF)_2$ after excitation of ν_1 and ν_2 have been reported as 17±1 ns and 0.48±0.05 ns, respectively.[34]

Conclusion

The vibrational predissociation dynamics of $(HCl)_2$ after HCl stretch overtone excitation has been studied using velocity-map ion imaging and 2+1 REMPI detection of monomer products. IR action spectra show features assigned to the free ($2\nu_1$) and bound ($2\nu_2$) HCl stretch overtones, and a combination band involving the intermolecular van der Waals stretch mode ($2\nu_2+\nu_4$). 2+1 REMPI spectroscopy was used to detect HCl(J_1) predissociation products via the $V^1\Sigma^+$–$X^1\Sigma^+(16,1)$ and $F^1\Delta_2$–$X^1\Sigma^+(0,1)$ transitions and HCl(J_0) levels via an unidentified $^1\Sigma^+$ state, following IR excitation of both $2\nu_1$ and $2\nu_2$. Fragment speed distributions derived from ion images were used to obtain correlated product pair distributions, $P(J_0,J_1)$; all product pairs identified comprise one vibrationally excited and

one vibrational ground state HCl molecule, and the majority of pairs are formed with $J_1 > J_0$, regardless of which stretch overtone was excited. The measurements support a dimer dissociation energy of D_0 = 397±7 cm^{-1}, which is smaller than previously reported values. A strong propensity to minimize the translational energy release accompanies overtone predissociation, with $f_T < 0.02$. Detailed analysis of the pair-correlated rotational distributions suggests that the predissociation dynamics are vibrational mode-dependent. The specificity is modest but appears to be characteristic of overtone excitation and distinct from the mode-independent predissociation dynamics observed following fundamental excitation of $(HCl)_2$. The LM→AM model has been used to rationalize the product pair state distribution qualitatively. Further calculations would be required to test its ability to describe the experimental observations quantitatively.

Acknowledgements

This material is based in part upon work supported by the National Science Foundation under Grant No. CHE-1566064. Acknowledgment is made to the Donors of the American Chemical Society Petroleum Research Fund for support of this research. We are grateful to Sergey Nizkorodov for allowing us to borrow various components of his working laser system.

References

(1) Nesbitt, D. J. High-Resolution Infrared Spectroscopy of Weakly Bound Molecular Complexes. *Chem. Rev.* **1988**, *88* (6), 843–870. https://doi.org/10.1021/cr00088a003.

(2) Nesbitt, D. J. High-Resolution, Direct Infrared Laser Absorption Spectroscopy in Slit Supersonic Jets: Intermolecular Forces and Unimolecular Vibrational Dynamics in Clusters. *Annu. Rev. Phys. Chem.* **1994**, *45* (1), 367–399. https://doi.org/10.1146/annurev.pc.45.100194.002055.

(3) Wormer, P. E. S.; van der Avoird, A. Intermolecular Potentials, Internal Motions, and Spectra of van Der Waals and Hydrogen-Bonded Complexes. *Chem. Rev.* **2000**, *100* (11), 4109–4144. https://doi.org/10.1021/cr990046e.

(4) Oudejans, L.; Miller, R. E. Photofragment Translational Spectroscopy of Weakly Bound Complexes: Probing the Interfragment Correlated Final State Distributions. *Annu. Rev. Phys. Chem.* **2001**, *52*, 607. https://doi.org/10.1146/annurev.physchem.52.1.607.

(5) Reisler, H. Photofragment Spectroscopy and Predissociation Dynamics of Weakly Bound Molecules. *Annu. Rev. Phys. Chem.* **2009**, *60* (1), 39–59. https://doi.org/10.1146/annurev.physchem.040808.090441.

(6) Samanta, A. K.; Wang, Y.; Mancini, J. S.; Bowman, J. M.; Reisler, H. Energetics and Predissociation Dynamics of Small Water, HCl, and Mixed HCl–Water Clusters. *Chem. Rev.* **2016**, *116* (9), 4913–4936. https://doi.org/10.1021/acs.chemrev.5b00506.

(7) Ohashi, N.; Pine, A. S. High Resolution Spectrum of the HCl Dimer. *J. Chem. Phys.* **1984**, *81* (1), 73–84. https://doi.org/10.1063/1.447355.

(8) Pine, A. S.; Howard, B. J. Hydrogen Bond Energies of the HF and HCl Dimers from Absolute Infrared Intensities. *J. Chem. Phys.* **1986**, *84* (2), 590–596. https://doi.org/10.1063/1.450605.

(9) Blake, G. A.; Busarow, K. L.; Cohen, R. C.; Laughlin, K. B.; Lee, Y. T.; Saykally, R. J. Tunable Far-infrared Laser Spectroscopy of Hydrogen Bonds: The K_a=0(u)→1(g) Rotation–Tunneling Spectrum of the HCl Dimer. *J. Chem. Phys.* **1988**, *89* (11), 6577–6587. https://doi.org/10.1063/1.455380.

(10) Blake, G. A.; Bumgarner, R. E. Direct Measurement of the HCl Dimer Tunneling Rate and Cl Isotope Dependence by Far-infrared Laser Sideband Spectroscopy of Planar Supersonic Jets. *J. Chem. Phys.* **1989**, *91* (11), 7300–7301. https://doi.org/10.1063/1.457298.

(11) Moazzen-Ahmadi, N.; McKellar, A. R. W.; Johns, J. W. C. The Far-Infrared Spectrum of the HCl Dimer. *J. Mol. Spectrosc.* **1989**, *138* (1), 282–301. https://doi.org/10.1016/0022-2852(89)90118-5.

(12) Moazzen-Ahmadi, N.; McKellar, A. R. W.; Jonhs, J. W. C. Far-Infrared Observations of Rotation-Tunneling and Torsional Transitions in the HCl Dimer. *Chem. Phys. Lett.* **1988**, *151* (4–5), 318–322. https://doi.org/10.1016/0009-2614(88)85142-X.

(13) Furlan, A.; Wülfert, S.; Leutwyler, S. Cars Spectra of the HCl Dimer in Supersonic Jets. *Chem. Phys. Lett.* **1988**, *153* (4), 291–295. https://doi.org/10.1016/0009-2614(88)80143-X.

(14) Schuder, M. D.; Lovejoy, C. M.; Lascola, R.; Nesbitt, D. J. High Resolution, Jet-Cooled Infrared Spectroscopy of $(HCl)_2$: Analysis of ν_1 and ν_2 HCl Stretching Fundamentals, Interconversion Tunneling, and Mode-Specific Predissociation Lifetimes. *J. Chem. Phys.* **1993**, *99* (6), 4346–4362. https://doi.org/10.1063/1.466089.

(15) Schuder, M. D.; Nesbitt, D. J. High Resolution near Infrared Spectroscopy of HCl–DCl and DCl–HCl: Relative Binding Energies, Isomer Interconversion Rates, and Mode Specific Vibrational Predissociation. *J. Chem. Phys.* **1994**, *100* (10), 7250–7267. https://doi.org/10.1063/1.466872.

(16) Schuder, M. D.; Lovejoy, C. M.; Nelson, D. D.; Nesbitt, D. J. Symmetry Breaking in HCl and DCl Dimers: A Direct Near-infrared Measurement of Interconversion Tunneling Rates. *J. Chem. Phys.* **1989**, *91* (7), 4418–4419. https://doi.org/10.1063/1.456774.

(17) Fárník, M.; Davis, S.; Nesbitt, D. J. Probing Hydrogen Bond Potential Surfaces for Out-of-Plane Geometries: Near-Infrared Combination Band Torsional (ν_6) Spectroscopy in $(HCl)_2$. *J. Chem. Phys.* **2003**, *118* (22), 10137–10148. https://doi.org/10.1063/1.1571822.
(18) Fárník, M.; Davis, S.; Schuder, M. D.; Nesbitt, D. J. Probing Potential Surfaces for Hydrogen Bonding: Near-Infrared Combination Band Spectroscopy of van Der Waals Stretch (ν_4) and Geared Bend (ν_5) Vibrations in $(HCl)_2$. *J. Chem. Phys.* **2002**, *116* (14), 6132–6145. https://doi.org/10.1063/1.1436105.
(19) Elrod, M. J.; Saykally, R. J. Determination of the Intermolecular Potential Energy Surface for $(HCl)_2$ from Vibration–Rotation–Tunneling Spectra. *J. Chem. Phys.* **1995**, *103* (3), 933–949. https://doi.org/10.1063/1.469794.
(20) Elrod, M. J.; Saykally, R. J. Vibration–Rotation–Tunneling Dynamics Calculations for the Four-dimensional $(HCl)_2$ System: A Test of Approximate Models. *J. Chem. Phys.* **1995**, *103* (3), 921–932. https://doi.org/10.1063/1.469793.
(21) Qiu, Y.; Bačić, Z. Exact Six-Dimensional Quantum Calculations of the Rovibrational Levels of $(HCl)_2$. *J. Chem. Phys.* **1997**, *106* (6), 2158–2170. https://doi.org/10.1063/1.473139.
(22) Qiu, Y.; Zhang, J. Z. H.; Bačić, Z. Six-Dimensional Quantum Calculations of Vibration-Rotation-Tunneling Levels of ν_1 and ν_2 HCl-Stretching Excited $(HCl)_2$. *J. Chem. Phys.* **1998**, *108* (12), 4804–4816. https://doi.org/10.1063/1.475891.
(23) Bunker, P. R.; Epa, V. C.; Jensen, P.; Karpfen, A. An Analytical Ab Initio Potential Surface and the Calculated Tunneling Energies for the HCl Dimer. *J. Mol. Spectrosc.* **1991**, *146* (1), 200–219. https://doi.org/10.1016/0022-2852(91)90383-L.
(24) Karpfen, A.; Bunker, P. R.; Jensen, P. An Ab Initio Study of the Hydrogen Chloride Dimer: The Potential Energy Surface and the Characterization of the Stationary Points. *Chem. Phys.* **1991**, *149* (3), 299–309. https://doi.org/10.1016/0301-0104(91)90029-S.
(25) Jensen, P.; Marshall, M. D.; Bunker, P. R.; Karpfen, A. An Ab Initio Close-Coupling Calculation of the Lower Vibrational Energies of the HCl Dimer. *Chem. Phys. Lett.* **1991**, *180* (6), 594–600. https://doi.org/10.1016/0009-2614(91)85016-P.
(26) Althorpe, S. C.; Clary, D. C.; Bunker, P. R. Calculation of the Far-Infrared Spectra for $(HF)_2$, $(HCl)_2$ and $(HBr)_2$. *Chem. Phys. Lett.* **1991**, *187* (4), 345–353. https://doi.org/10.1016/0009-2614(91)80264-X.
(27) Mancini, J. S.; Bowman, J. M. A New Many-Body Potential Energy Surface for HCl Clusters and Its Application to Anharmonic Spectroscopy and Vibration–Vibration Energy Transfer in the HCl Trimer. *J. Phys. Chem. A* **2014**, *118* (35), 7367–7374. https://doi.org/10.1021/jp412264t.
(28) Mancini, J. S.; Samanta, A. K.; Bowman, J. M.; Reisler, H. Experiment and Theory Elucidate the Multichannel Predissociation Dynamics of the HCl Trimer: Breaking Up Is Hard To Do. *J. Phys. Chem. A* **2014**, *118* (37), 8402–8410. https://doi.org/10.1021/jp5015753.
(29) Serafin, J.; Ni, H.; Valentini, J. J. Direct, Spectroscopic Measurement of the Rotational State Distribution of HCl Fragments from the Vibrational Predissociation of ν_2=1 $(HCl)_2$ Produced by Stimulated Raman Excitation. *J. Chem. Phys.* **1994**, *100* (3), 2385–2387. https://doi.org/10.1063/1.466483.
(30) Ni, H.; Serafin, J. M.; Valentini, J. J. Dynamics of the Vibrational Predissociation of HCl Dimer. *J. Chem. Phys.* **2000**, *113* (8), 3055–3066. https://doi.org/10.1063/1.1286975.
(31) Ni, H.; Serafin, J. M.; Valentini, J. J. State-resolved, Three-dimensional Product Recoil Velocity Spectroscopy. *J. Chem. Phys.* **1996**, *104* (6), 2259–2270. https://doi.org/10.1063/1.470922.
(32) Vissers, G. W. M.; Oudejans, L.; Miller, R. E.; Groenenboom, G. C.; van der Avoird, A. Vibrational Predissociation in the HCl Dimer. *J. Chem. Phys.* **2004**, *120* (20), 9487–9498. https://doi.org/10.1063/1.1711601.
(33) Bohac, E. J.; Marshall, M. D.; Miller, R. E. Initial State Effects in the Vibrational Predissociation of Hydrogen Fluoride Dimer. *J. Chem. Phys.* **1992**, *96* (9), 6681–6695. https://doi.org/10.1063/1.462578.

(34) Suhm, M. A.; Farrell, J. T.; McIlroy, A.; Nesbitt, D. J. High Resolution 1.3 Mm Overtone Spectroscopy of HF Dimer in a Slit Jet: K_a=0←0 and K_a=1←0 Subbands of v_{acc}=2←0. *J. Chem. Phys.* **1992**, *97* (8), 5341–5354. https://doi.org/10.1063/1.463794.
(35) Liu, K.; Dulligan, M.; Bezel, I.; Kolessov, A.; Wittig, C. Quenching of Interconversion Tunneling: The Free HCl Stretch First Overtone of $(HCl)_2$. *J. Chem. Phys.* **1998**, *108* (23), 9614–9616. https://doi.org/10.1063/1.476436.
(36) Chang, H.; Klemperer, W. The Vibrational Second Overtones of HF Dimer: A Quartet. *J. Chem. Phys.* **1994**, *100* (1), 1–14. https://doi.org/10.1063/1.466980.
(37) Chang, H.; Klemperer, W. State-specific Vibrational Predissociation and Interconversion Tunneling Quenching at $3\nu_1$ and $3\nu_2$ of $(HF)_2$. *J. Chem. Phys.* **1993**, *98* (12), 9266–9278. https://doi.org/10.1063/1.464407.
(38) von Puttkamer, K.; Quack, M. Vibrational Spectra of $(HF)_2$, $(HF)_n$ and Their D-Isotopomers: Mode Selective Rearrangements and Nonstatistical Unimolecular Decay. *Chem. Phys.* **1989**, *139* (1), 31–53. https://doi.org/10.1016/0301-0104(89)90003-7.
(39) Liu, K.; Kolessov, A.; Partin, J. W.; Bezel, I.; Wittig, C. Probing the Cl–HCl Complex via Bond-Specific Photodissociation of $(HCl)_2$. *Chem. Phys. Lett.* **1999**, *299* (5), 374–380. https://doi.org/10.1016/S0009-2614(98)01293-7.
(40) Picconatto, C. A.; Ni, H.; Srivastava, A.; Valentini, J. J. Quantum State Distributions of HCl from the Ultraviolet Photodissociation of HCl Dimer. *J. Chem. Phys.* **2001**, *114* (16), 7073–7080. https://doi.org/10.1063/1.1360786.
(41) Toulson, B. W.; Alaniz, J. P.; Hill, J. G.; Murray, C. Near-UV Photodissociation Dynamics of CH_2I_2. *Phys. Chem. Chem. Phys.* **2016**, *18* (16), 11091–11103. https://doi.org/10.1039/C6CP01063F.
(42) Roberts, G. M.; Nixon, J. L.; Lecointre, J.; Wrede, E.; Verlet, J. R. R. Toward Real-Time Charged-Particle Image Reconstruction Using Polar Onion-Peeling. *Rev. Sci. Instrum.* **2009**, *80* (5), 053104. https://doi.org/10.1063/1.3126527.
(43) *PGOPHER, a Program for Simulating Rotational Structure, C. M. Western, University of Bristol, Http://Pgopher.Chm.Bris.Ac.Uk*; PGOPHER, a Program for Simulating Rotational Structure, C. M. Western, University of Bristol, http://pgopher.chm.bris.ac.uk.
(44) Green, D. S.; Bickel, G. A.; Wallace, S. C. (2 + 1) Resonance Enhanced Multiphoton Ionization of Hydrogen Chloride in a Pulsed Supersonic Jet: Vacuum Wavenumbers of Rotational Lines with Detailed Band Analysis for Excited Electronic States of $H^{35}Cl$. *J. Mol. Spectrosc.* **1991**, *150* (2), 388–469. https://doi.org/10.1016/0022-2852(91)90240-B.
(45) Rank, D. H.; Rao, B. S.; Wiggins, T. A. Molecular Constants of HCl^{35}. *J. Mol. Spectrosc.* **1965**, *17* (1), 122–130. https://doi.org/10.1016/0022-2852(65)90114-1.
(46) Webb, D. U.; Rao, N. K. Vibration Rotation Bands of Heated Hydrogen Halides. *J. Mol. Spectrosc.* **1968**, *28* (2), 121–124. https://doi.org/10.1016/0022-2852(68)90001-5.
(47) Rudić, S.; Ascenzi, D.; Orr-Ewing, A. J. Rotational Distribution of the HCl Products from the Reaction of $Cl(^2P)$ Atoms with Methanol. *Chem. Phys. Lett.* **2000**, *332* (5–6), 487–495. https://doi.org/10.1016/S0009-2614(00)01312-9.
(48) Rudić, S.; Murray, C.; Ascenzi, D.; Anderson, H.; Harvey, J. N.; Orr-Ewing, A. J. The Dynamics of Formation of HCl Products from the Reaction of Cl Atoms with Methanol, Ethanol, and Dimethyl Ether. *J. Chem. Phys.* **2002**, *117* (12), 5692–5706. https://doi.org/10.1063/1.1502646.
(49) Korolik, M.; Arnold, D. W.; Johnson, M. J.; Suchan, M. M.; Reisler, H.; Wittig, C. Trapping-Desorption and Direct-Inelastic Scattering of HCl from MgO(100). *Chem. Phys. Lett.* **1998**, *284* (3), 164–170. https://doi.org/10.1016/S0009-2614(97)01421-8.
(50) Lykke, K. R.; Kay, B. D. Rotationally Inelastic Gas–Surface Scattering: HCl from Au(111). *J. Chem. Phys.* **1990**, *92* (4), 2614–2623. https://doi.org/10.1063/1.457955.

(51) Toulson, B. W.; Fishman, D. A.; Murray, C. Photodissociation Dynamics of Acetone Studied by Time-Resolved Ion Imaging and Photofragment Excitation Spectroscopy. *Phys. Chem. Chem. Phys.* **2018**, *20* (4), 2457–2469. https://doi.org/10.1039/C7CP07320H.
(52) Jensen, P.; Bunker, P. R.; Epa, V. C.; Karpfen, A. An Ab Initio Calculation of the Fundamental and Overtone HCl Stretching Vibrations for the HCl Dimer. *J. Mol. Spectrosc.* **1992**, *151* (2), 384–395. https://doi.org/10.1016/0022-2852(92)90574-8.
(53) Anderson, D. T.; Davis, S.; Nesbitt, D. J. Probing Hydrogen Bond Potentials via Combination Band Spectroscopy: A near Infrared Study of the Geared Bend/van Der Waals Stretch Intermolecular Modes in $(HF)_2$. *J. Chem. Phys.* **1996**, *104* (16), 6225–6243. https://doi.org/10.1063/1.471285.
(54) Ni, H.; Serafin, J. M.; Valentini, J. J. A Simple Method for Measurement of the Full Three-Dimensional Velocity Distribution of Photofragments and Reaction Products. *Chem. Phys. Lett.* **1995**, *244* (3–4), 207–212. https://doi.org/10.1016/0009-2614(95)00926-U.
(55) Ewing, G. E. Selection Rules for Vibrational Energy Transfer: Vibrational Predissociation of van Der Waals Molecules. *J. Phys. Chem.* **1987**, *91* (18), 4662–4671. https://doi.org/10.1021/j100302a008.
(56) Baer, T.; Hase, W. L. *Unimolecular Reaction Dynamics: Theory and Experiments*; Oxford University Press, 1996.
(57) Ch'ng, L. C.; Samanta, A. K.; Czakó, G.; Bowman, J. M.; Reisler, H. Experimental and Theoretical Investigations of Energy Transfer and Hydrogen-Bond Breaking in the Water Dimer. *J. Am. Chem. Soc.* **2012**, *134* (37), 15430–15435. https://doi.org/10.1021/ja305500x.
(58) McCaffery, A. J. A New Approach to Molecular Collision Dynamics. *Phys. Chem. Chem. Phys.* **2004**, *6* (8), 1637–1657. https://doi.org/10.1039/B316161G.
(59) McCaffery, A. J.; Marsh, R. J. Vibrational Predissociation of van Der Waals Molecules: An Internal Collision, Angular Momentum Model. *J. Chem. Phys.* **2002**, *117* (20), 9275–9285. https://doi.org/10.1063/1.1516791.
(60) Pritchard, M.; Parr, J.; Li, G.; Reisler, H.; McCaffery, A. J. The Mechanism of H-Bond Rupture: The Vibrational Pre-Dissociation of C_2H_2–HCl and C_2H_2–DCl. *Phys. Chem. Chem. Phys.* **2007**, *9* (47), 6241–6252. https://doi.org/10.1039/B710967A.
(61) Sampson, R. K.; Bellm, S. M.; McCaffery, A. J.; Lawrance, W. D. Rotational Distributions Following van Der Waals Molecule Dissociation: Comparison between Experiment and Theory for Benzene–Ar. *J. Chem. Phys.* **2005**, *122* (7), 074311. https://doi.org/10.1063/1.1847512.
(62) McCaffery, A. J.; Pritchard, M.; Reisler, H. Can the Fragmentation of Hydrogen-Bonded Dimers Be Predicted: Predissociation of C_2H_2–HX. *J. Phys. Chem. A* **2010**, *114* (9), 2983–2990. https://doi.org/10.1021/jp904793d.
(63) Marsh, R. J.; McCaffery, A. J. Rotational Transfer in Diatom-Diatom Collisions. *Chem. Phys. Lett.* **2001**, *335* (1–2), 134–139. https://doi.org/10.1016/S0009-2614(01)00022-7.
(64) Le Roy, R. J. RKR1: A Computer Program Implementing the First-Order RKR Method for Determining Diatomic Molecule Potential Energy Functions. *J. Quant. Spectrosc. Rad. Trans.* **2017**, *186*, 158–166. https://doi.org/10.1016/j.jqsrt.2016.03.030.
(65) Valiev, M.; Bylaska, E. J.; Govind, N.; Kowalski, K.; Straatsma, T. P.; Van Dam, H. J. J.; Wang, D.; Nieplocha, J.; Apra, E.; Windus, T. L.; de Jong, W. A. NWChem: A Comprehensive and Scalable Open-Source Solution for Large Scale Molecular Simulations. *Comp. Phys. Comm.* **2010**, *181* (9), 1477–1489. https://doi.org/10.1016/j.cpc.2010.04.018.
(66) Whiteley, T. W. J.; McCaffery, A. J. Angular Momentum Analysis of Rotational Transfer of Superthermal Relative Velocity Distributions. *J. Phys. B: At. Mol. Opt. Phys.* **1996**, *29* (24), 6133–6141. https://doi.org/10.1088/0953-4075/29/24/019.

Tables

Table 1 Product pair populations and uncertainties (1σ) derived from the ion images and REMPI spectroscopy.

(J_0,J_1)	$P(J_0,J_1)$ $2\nu_1$	$P(J_0,J_1)$ $2\nu_2$
(2,14)	3.6±1.0	9.2±2.7
(3,14)	17.1±3.0	31.4±8.0
(4,14)	25.8±4.4	–
(4,13)	1.0±0.3	2.7±0.7
(5,13)	2.5±0.6	3.1±0.8
(6,13)	17.3±3.5	33.0±8.7
(6,12)	0.3±0.2	1.2±0.5
(7,12)	6.3±2.0	8.8±3.4
(8,12)	8.6±2.7	–
(7,11)	0.6±0.2	1.2±0.5
(8,11)	2.5±0.7	1.4±0.5
(9,11)	2.8±0.8	3.3±1.3
(10,7)	–	0.1±0.1
(10,8)	0.1±0.1	0.3±0.2
(10,9)	0.3±0.1	0.1±0.1
(11,7)	0.2±0.1	0.3±0.2
(11,8)	0.8±0.3	1.3±0.7
(11,9)	3.2±0.9	0.1±0.1
(12,7)	0.9±0.3	0.4±0.3
(13,3)	0.5±0.2	0.2±0.1
(13,4)	1.0±0.4	0.5±0.2
(13,5)	3.3±1.3	1.3±0.6
(13,6)	1.4±0.6	

Table 2 Summary of quantities determined form product rotational distributions for predissociation of $(HCl)_2$ after excitation of $2\nu_1$ and $2\nu_2$. Shown are available energies (E_{AVL}), average product recoil translational energy ($\langle E_T \rangle$), fraction partitioned into translation (f_T), average product rotational quantum numbers formed in v = 0, 1 ($\langle J_0 \rangle$, $\langle J_1 \rangle$), and the average difference ($\langle \Delta J \rangle$).

	$2\nu_1$	$2\nu_2$
E_{AVL} / cm^{-1}	5259±7	5199±7
$\langle E_T \rangle$ / cm^{-1}	91±82	68±77
f_T	0.017±0.016	0.013±0.015
$\langle J_1 \rangle$	12.4±2.4	12.9±1.7
$\langle J_0 \rangle$	5.9±2.9	5.1±2.4
$\langle \lvert \Delta J \rvert \rangle$	7.9±2.9	8.3±2.8

840 Table 3 Ellipse parameter a, the length of the semi-major axis evaluated at the outer
841 turning point of the RKR potential for various vibrational levels; the length of the
842 semi-minor axis is $b = a/2$. Also shown are the maximum torque-arm, $b_{\mathrm{n}}^{\mathrm{max}}$, values
843 for the donor (impulse at H) and the acceptor (impulse at Cl). Values in parenthesis
844 were evaluated at the equilibrium geometry.

	a / Å	$b_{\mathrm{n,d}}^{\mathrm{max}}$ / Å	$b_{\mathrm{n,a}}^{\mathrm{max}}$ / Å
$v = 2$	1.57	0.95 (0.73)	0.26 (0.07)
$v = 1$	1.50	0.97 (0.80)	0.25 (0.07)
$v = 0$	1.39	1.00 (0.82)	0.22 (0.06)
r_{e}	1.29	1.03 (0.85)	0.19 (0.07)

845

846

Figures

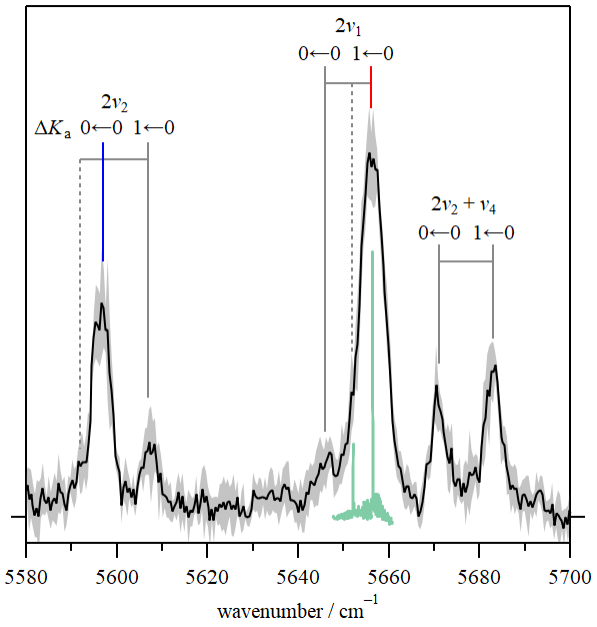

Figure 1 IR action spectrum of $(HCl)_2$ obtained probing $H^{35}Cl(J_1 = 12)$ predissociation products. Solid and dashed ladders indicate bands due to the $(H^{35}Cl)_2$ homodimer and the $H^{35}Cl–H^{37}Cl$ heterodimer, respectively. The $2\nu_2$ transition at 5597 cm^{-1} (blue) and the $2\nu_1$ transition at 5656 cm^{-1} (red) were excited for imaging measurements. Also shown in green is the high-resolution cavity ring-down spectrum recorded by Liu *et al.*[31]

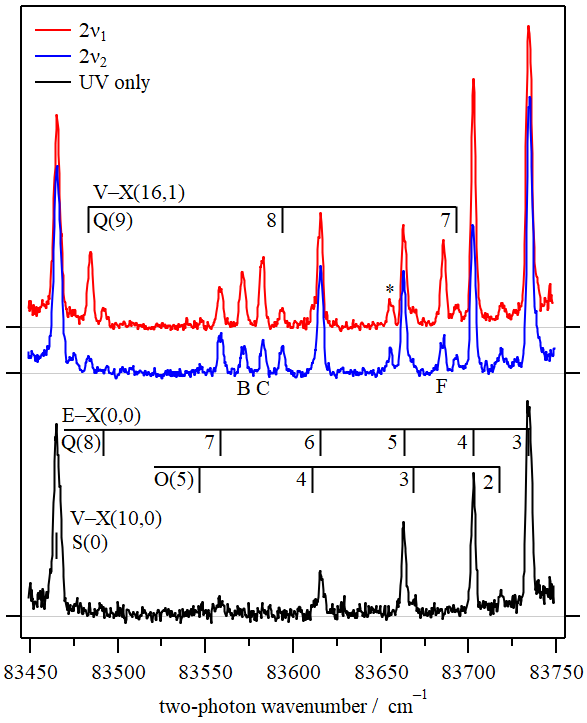

Figure 2 2+1 REMPI spectra of a section of the HCl $E^1\Sigma^+$–$X^1\Sigma^+$(0,0) Q-branch recorded on the m/z = 36 ($H^{35}Cl^+$) channel. The UV only spectrum (black) shows signal due to residual HCl monomer present in the molecular beam. The upper spectra were recorded with the IR pump tuned to either the $2\nu_1$ band at 5656 cm^{-1} (red) or the $2\nu_2$ band at 5597 cm^{-1} (blue). The IR+UV spectra contain additional spectral lines and show enhancement of some E–X(0,0) transitions. Assignments are made based on known HCl spectroscopy and analysis of speed distributions obtained from ion images. The transitions marked with asterisks have not been identified.

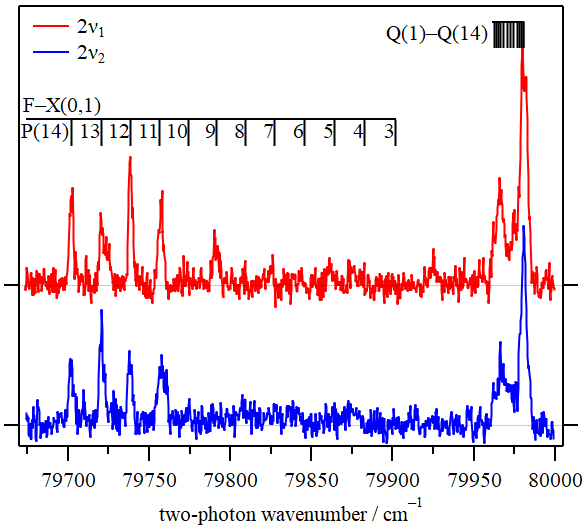

Figure 3 2+1 REMPI spectra of the HCl $F^1\Delta_2$–$X^1\Sigma^+$(0,1) band. No UV only signal was observed in this region. The spectra were recorded with the IR pump tuned to either the $2\nu_1$ band at 5656 cm^{-1} (red) or the $2\nu_2$ band at 5597 cm^{-1} (blue).

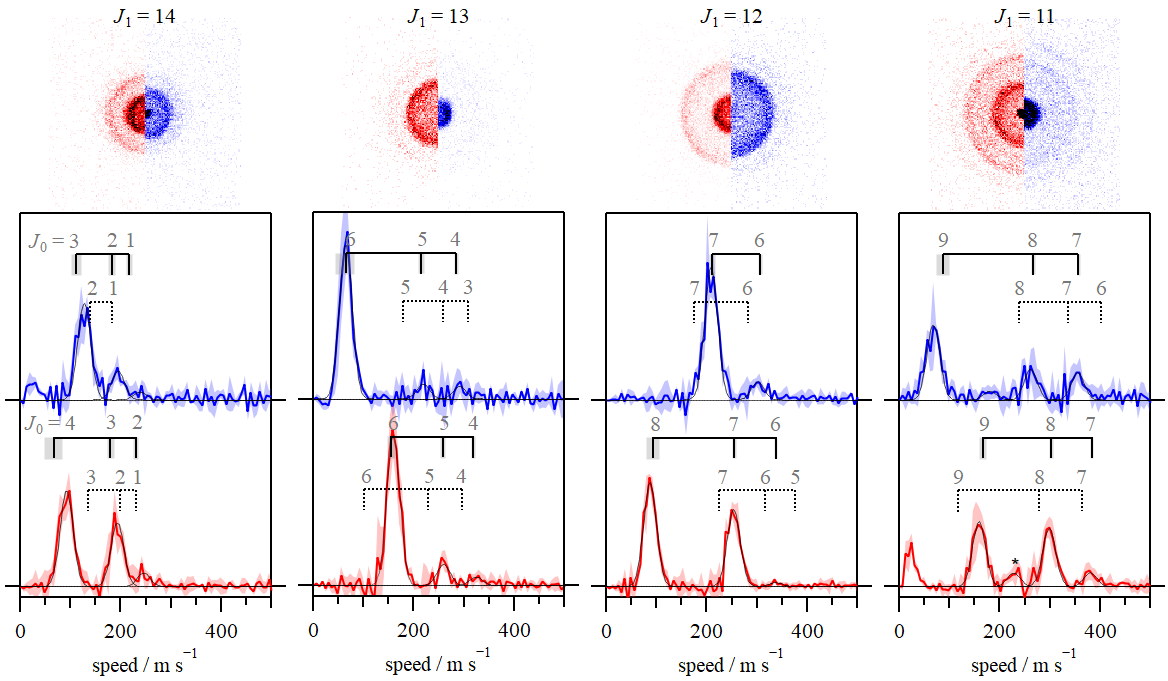

Figure 4 Ion images and normalized speed distributions obtained probing HCl(J_1) predissociation products on the F–X(0,1) transition following predissociation of $(HCl)_2$ via the $2\nu_1$ (red) and $2\nu_2$ (blue) modes. Fits to Gaussian functions are shown in black. Vertical ladders mark the maximum speed calculated for formation of the partner fragment in the specified J_0 levels. Solid and dashed ladders represent speeds calculated using our experimental value of D_0 = 397±7 cm^{-1} and the previously reported value of D_0 = 439 cm^{-1}, respectively. Shaded regions represent 1σ standard deviations. Features marked with asterisks originate from overlapping REMPI transitions.

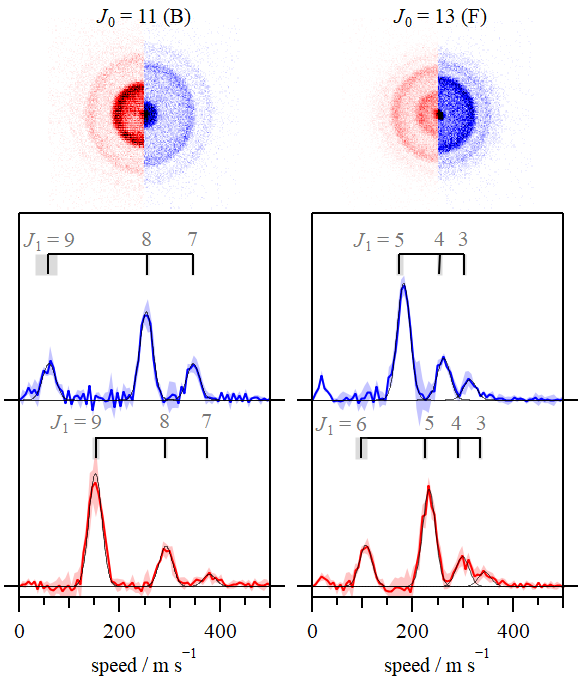

Figure 5 Ion images and normalized speed distributions of HCl product lines B and F (shown in Figure 2) resulting from the predissociation of $(HCl)_2$ following excitation on the $2\nu_1$ (red) and $2\nu_2$ (blue) bands. Lines B and F have been assigned to HCl(J_0=11) and HCl(J_0 =13), respectively. See text for discussion. Horizontal ladders mark the speeds for formation of the partner fragment in specified J_1 levels calculated using D_0 = 397±7 cm^{-1}. Shaded regions represent 1σ standard deviations.

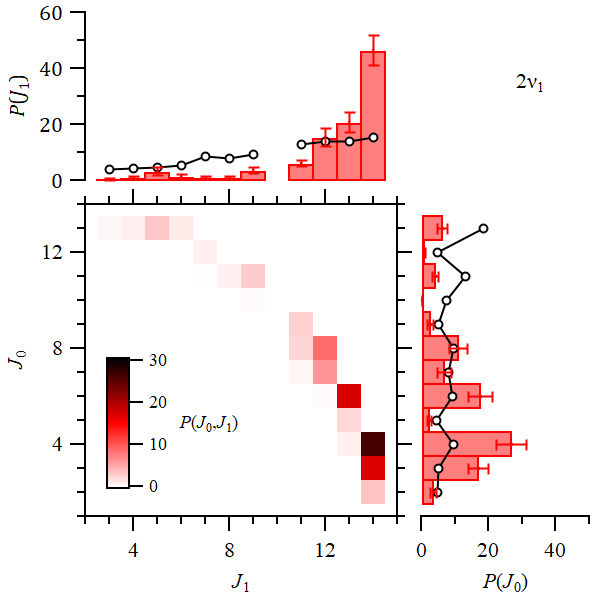

Figure 6 Correlated product pair population distributions $P(J_0,J_1)$ after excitation of $(HCl)_2$ on the $2\nu_1$ band. The total population has been normalized to 100. Horizontal and vertical bars show the total rotational population distributions in $v = 0$ and $v = 1$, $P(J_0)$ and $P(J_1)$, respectively, after summation over all co-fragment levels. Black circles represent the normalized populations calculated using an energy-gap model (see text for details). Error bars represent 1σ uncertainties.

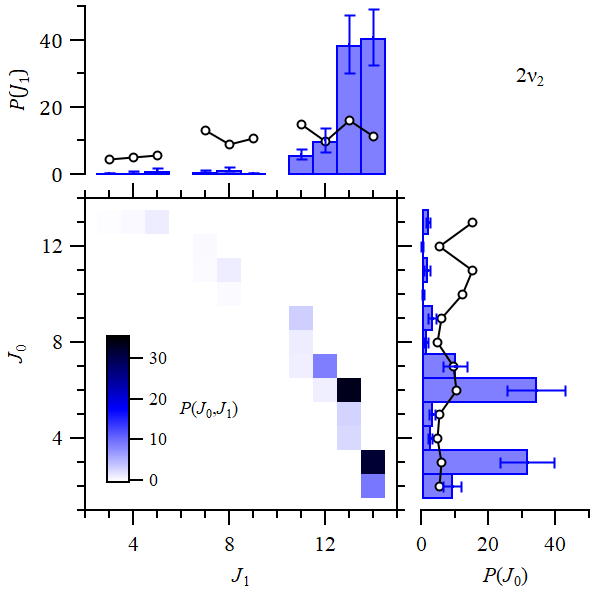

Figure 7 Correlated product pair population distributions $P(J_0,J_1)$ after excitation of $(HCl)_2$ on the $2\nu_2$ band. The total population has been normalized to 100. Horizontal and vertical bars show the total rotational population distributions in $v = 0$ and $v = 1$, $P(J_0)$ and $P(J_1)$, respectively, after summation over all co-fragment levels. Black circles represent the normalized populations calculated using an energy-gap model (see text for details). Error bars represent 1σ uncertainties.

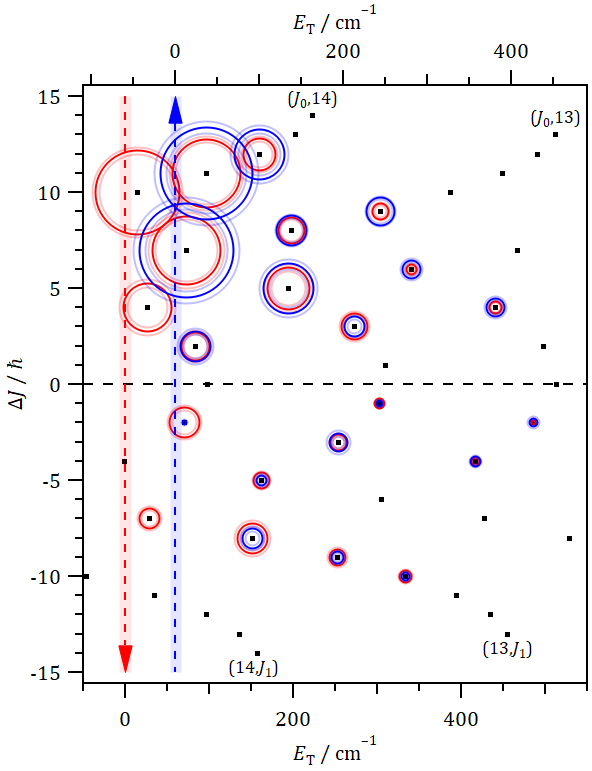

Figure 8 Product pair population distributions plotted as $\Delta J = J_1 - J_0$ against recoil translational energy, E_T, after excitation of $2\nu_1$ (red, bottom axis) and $2\nu_2$ (blue, top axis). The areas of the circles are proportional to populations and the fainter outer circles represent the uncertainty range (1σ). Dots (black) indicate the locations of all energetically accessible product pairs. The horizontal axes are offset such that pairs with the same (J_0, J_1) values overlap.

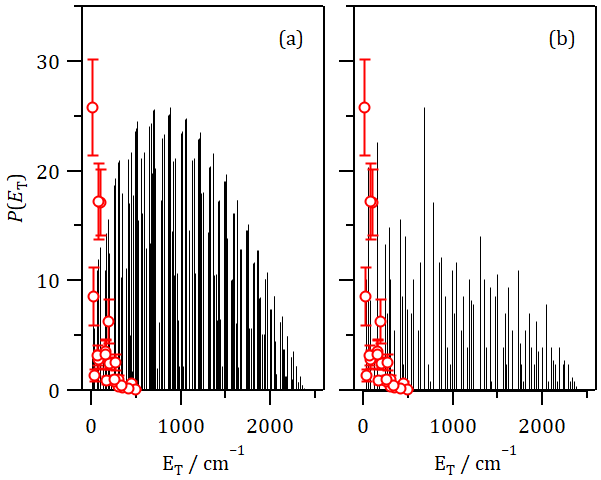

914

915 Figure 9 Comparison of experimental product pair population distribution following
916 $2\nu_1$ excitation (red circles) plotted against translational energy, E_T, with (a) statistical
917 prior and (b) phase space theory distributions. The calculated distributions have
918 been normalized to have the same maximum value as the experimental distribution.

919

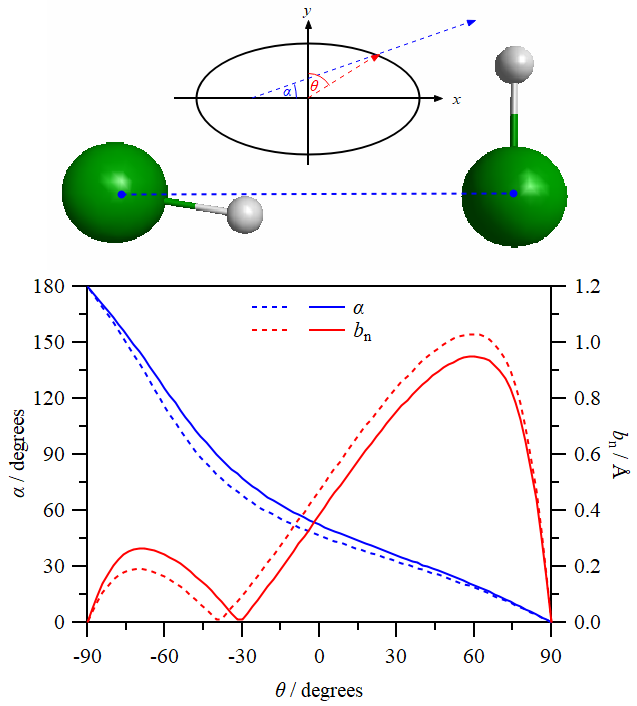

Figure 10 Top: $(HCl)_2$ geometry and internal coordinates for hard ellipse model. Each HCl monomer is modeled as an ellipse, centered at the midpoint of the bond. The semi-major and semi-minor axes are defined such that $a = 2b$, where a is chosen to be the outer turning point for $v = 2$ or the equilibrium bond length. The blue dashed line represents an assumed recoil vector that connects the centers of mass for each HCl molecule; α is the angle between an HCl bond and the recoil vector. The effective torque-arm, b_n is calculated from the angle θ as described in the text. θ = +90° is the H-atom end of the molecule, θ = −90° is the Cl-atom end. Bottom: Plot showing variation of angle α (blue) and effective torque-arm (red) with angle θ. Solid lines correspond to calculations using $a = r_{max}(v = 2)$ and dashed lines for $a = r_e$.

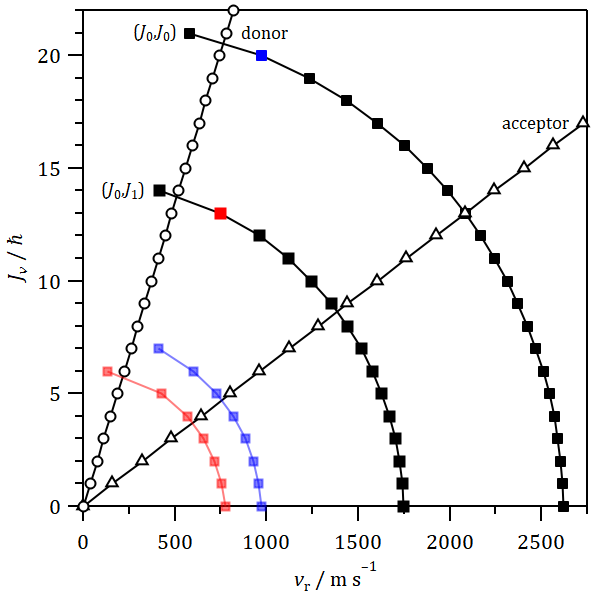

Figure 11 Velocity-angular momentum plots for vibrational predissociation of $(HCl)_2$ after excitation of the H-bond donor stretch overtone, $2\nu_2$. E-plots for individual monomers are represented as filled squares for (J_0,J_0) and (J_0,J_1) product pairs where one fragment is in $J = 0$. A-plots are calculated for the H-bond donor and acceptor moieties using both optimum values of b_n^{max} for the donor (open circles) and acceptor (open triangles). Reduced E-plots are also shown for a (J_0,J_0) pair where one fragment is in $J = 20$ (blue) and a (J_0,J_1) pair where one fragment is in $J = 13$ (red).